Modulation of Tropical Cyclones over the Eastern Pacific by the Intraseasonal Variability Simulated in an AGCM

XIANAN JIANG[1,2], MING ZHAO[3], and DUANE E. WALISER[2]

[1]*Joint Institute for Regional Earth System Science & Engineering, University of California, Los Angeles, California*

[2]*Jet Propulsion Laboratory, California Institute of Technology, Pasadena, California*

[3]*NOAA/Geophysical Fluid Dynamics Laboratory, Princeton, New Jersey*

Submitted 09/15/11, Journal Climate
Revised 02/13/12

Corresponding author address: Dr. Xianan Jiang, Jet Propulsion Laboratory, California Institute of Technology, MS 233-300, 4800 Oak Grove Drive, Pasadena, CA 91109. Email: xianan@jifresse.ucla.edu.

Abstract

This study illustrates that observed modulations of tropical cyclone (TC) genesis over the eastern Pacific (EPAC) by large-scale intraseasonal variability (ISV) are represented well in a recently developed high-resolution atmospheric model (HiRAM) at NOAA's Geophysical Fluid Dynamics Laboratory (GFDL) with a horizontal resolution of about 50km. Considering the intrinsic predictability of the ISV of 2-4 weeks, this analysis thus has significant implications for dynamically based TC predictions on intraseasonal time scales. Analysis indicates that the genesis potential index (GPI) anomalies associated with the ISV can generally well depict ISV modulations of EPAC TC genesis in both observations and HiRAM simulations. Further investigation is conducted to explore the key factors associated with ISV modulation of TC activity based on an analysis of budget terms of the observed GPI during the ISV life cycle. It is found that, while relative roles of GPI factors are dependent on ISV phase and location, lower-level cyclonic vorticity, enhanced mid-level relative humidity, and reduced vertical wind shear can all contribute to the observed active TC genesis over the EPAC during particular ISV phases. In general, the observed anomalous ISV patterns of these large-scale GPI factors are well represented in HiRAM. Model deficiencies are also noted particularly in the anomalous mid-level relative humidity patterns and amplitude of vertical wind shear associated with the EPAC ISV.

1. Introduction

Due to the great threat of tropical cyclones (TCs) to life and property worldwide, improving prediction of TC activity has profound socio-economic impacts. While short- and medium-range forecasts (up to one week) and seasonal outlooks of TC activity have been routinely conducted, predictions of TCs on intraseasonal time scales (one week to several weeks) are still at an experimental stage in most operational prediction centers[1]. This is largely due to our limited understanding of predictability sources for TC prediction on this intermediate time scale. For short-

[1] Intraseasonal TC forecasts have been operational at the European Centre for Medium-Range Weather Forecasts (ECMWF) since January 2011.

to-medium range TC forecasts, the skill is essentially from the initial condition, and forecasts are usually realized by integrating high-resolution, in some cases limited-area, dynamical models with sophisticated data assimilation systems. Moreover, the predictability of seasonal TC forecasts is largely dependent on slowly varying large-scale elements, such as sea surface temperature (SST; e.g., Gray 1984; Shapiro 1987; Goldenberg and Shapiro 1996). For TC prediction on the intraseasonal time scale, predictability is generally considered rooted in the tropical intraseasonal variability (ISV, e.g., Madden-Julian Oscillation, Madden and Julian 1994), although SST and other tropical waves could also provide partial predictability (e.g., Leroy and Wheeler 2008; Frank and Roundy 2006). The significant impacts of the ISV on TC genesis and movement over various ocean basins have been widely reported (e.g., *Western Pacific*: Nakazawa 1988; Liebmann et al. 1994; Wang and Zhou 2008; *Indian Ocean*: Bessafi and Wheeler 2006; Ho et al. 2006; Kikuchi and Wang 2010; *Eastern Pacific*: Molinari et al. 1997; Maloney and Hartmann 2000b; Aiyyer and Molinari 2008; *Gulf of Mexico*: Maloney and Hartmann 2000a; Mo 2000; Higgins and Shi 2001; *Atlantic Ocean*: Maloney and Shaman 2008; Klotzbach 2010; Camargo et al. 2007b; *Australian Region*: Ho et al. 2006). It is found that the frequency of TC genesis during convectively active ISV phases is up to four times that during suppressed ISV phases (e.g., Maloney and Hartmann 2000a; Barrett and Leslie 2009). Due to this intimate linkage between the ISV and TC activity, and considering the intrinsic predictability of the ISV of 2-4 weeks (Waliser 2006), the reliable prediction of the ISV state several weeks ahead will provide an important foundation for TC prediction on intraseasonal time scales.

While significant progress over the past 2-3 decades has been made in understanding the fundamental physics of the ISV (Zhang 2005; Lau and Waliser 2011), achieving credible ISV simulations with general circulation models (GCMs) has been challenging (e.g., Slingo et al. 1996; Waliser et al. 2003; Lin et al. 2006; Kim et al. 2009; Jiang et al. 2011). Until recently, useful predictive skill of the ISV had generally been limited to only 1–2 weeks, with statistical models often outperforming dynamical models (e.g., Waliser 2006; Jiang et al. 2008). This becomes one of

88 the main reasons that current intraseasonal TC predictions, although still limited, are mainly based
89 on statistical approaches (e.g., Frank and Roundy 2006; Leroy and Wheeler 2008). However, in
90 recent years, the improvements in model physics, spatial resolution and data assimilation systems
91 have led to significant increases in the predictive skill for ISV in a few models (Waliser 2011). For
92 example, the ECMWF Integrated Forecast System (IFS; Bechtold et al. 2008; Vitart and Molteni
93 2010), NCEP Coupled Forecast System v2 (Zhang and v. d. Dool 2011) and the Predictive Ocean-
94 Atmosphere Model for Australia (Rashid et al. 2011), exhibit useful ISV predictive skill out to 2-4
95 weeks. This improved skill, along with the resolutions to reasonably resolve TCs, motivated Vitart
96 (2009) to analyze the ISV-TC connections in a set of 46-day hindcasts based on a recent version of
97 the ECMWF IFS with a horizontal resolution of 80km. Vitart (2009) demonstrated that the
98 ECMWF forecast model is generally capable of depicting the observed modulations of the ISV on
99 TC activity including genesis and risk of landfall. This study, for the first time, illustrates that it is
100 possible for a conventional cumulus-parameterized global model to represent both ISV and TCs, as
101 well as their intimate relationships, thus suggesting a plausible new dynamical approach for
102 intraseasonal TC forecasts. Inspired by this encouraging work, there has been increasing enthusiasm
103 in exploring the predictive skill and predictability of dynamical TC forecasts based on ECMWF IFS
104 hindcasts / forecasts (e.g., Belanger et al. 2010; Vitart et al. 2010; Elsberry et al. 2010).

105 In this study, we present results from an analysis of the ISV-TC relationships over the eastern
106 Pacific (EPAC) as simulated in a high resolution GCM (hereafter HiRAM) recently developed at
107 National Oceanic and Atmospheric Administration (NOAA)'s Geophysical Fluid Dynamics
108 Laboratory (GFDL; Zhao et al. 2009). In the EPAC, the ITCZ and warm SST are generally
109 confined north of the equator, particularly in boreal summer, with the warm water region often
110 referred to as the EPAC warm pool. Most TCs over the EPAC are spawned over this warm pool
111 region. The EPAC ITCZ also exhibits vigorous intraseasonal variations in winds and convection
112 (Knutson and Weickmann 1987; Kayano and Kousky 1999; Maloney and Esbensen 2003, 2007; de
113 Szoeke and Bretherton 2005; Jiang and Waliser 2008, 2009; Jiang et al. 2011), which exert broad

impacts on regional weather and short-term climate (e.g., Magana et al. 1999; Higgins and Shi 2001; Lorenz and Hartmann 2006; Small et al. 2007; Wu et al. 2009; Serra et al. 2010; Martin and Schumacher 2010), including TC activity over the EPAC and the Gulf of Mexico as mentioned earlier. Two dominant ISV periodicities, e.g., a 40-day variability mode and a quasi-biweekly mode, were reported over the EPAC (Jiang and Waliser 2009). A recent multi-model evaluation study by Jiang et al. (2011) illustrates that HiRAM is one of the best in depicting both dominant EPAC ISV modes among nine GCMs analyzed. Moreover, at a horizontal resolution of about 50km, HiRAM also shows great potential in representing global TC activity, including its climate distribution, interannual and multi-decadal variability, as well as responses to global warming (Zhao et al. 2009; Zhao and Held 2010; Held and Zhao 2011).

As HiRAM is capable of capturing both the ISV and TC activity over the EPAC, it is of great interest to explore how observed ISV-TC relationships are depicted in this model. This study, on one hand, will have significant implications on the intraseasonal dynamical TC forecasts as discussed earlier. Moreover, it is noted that ECMWF IFS hindcasts analyzed by Vitart (2009) were initialized by observations; thus, skill could be gained from the specified initial conditions. In the present study, integrations from a long-term climatological run based on HiRAM are analyzed.

2. Model, Datasets, and Approaches

Simulations from 1998 to 2008 based on GFDL HiRAM analyzed in this study are similar to those utilized in Zhao et al. (2009) with a horizontal resolution of 50km and prescribed observed monthly mean sea surface temperatures (SSTs) and sea ice. Model storms are detected and tracked every six hours following the algorithm described in Zhao et al. (2009). At each time, a potential tropical storm is identified by a local 850hPa relative vorticity maximum exceeding 1.6×10^{-4} s^{-1}, a minimum in sea surface pressure, a maximum in near-surface wind speed greater than $17ms^{-1}$, and a warm core structure with maximum temperature between 300 and 500hPa. Daily rainfall output from HiRAM is employed to identify EPAC ISV events. Additionally, daily 3D winds, relative

139 humidity, and temperature fields from HiRAM are also analyzed to explore key factors associated
140 with the ISV in modulating TC genesis in model simulations.

141 Six-hourly tropical storm "best tracks" over the EPAC and Atlantic Ocean from 1998 to 2008
142 are obtained from the hurricane database (HURDAT) maintained by the NOAA National Hurricane
143 Center (Jarvinen et al. 1984). Rainfall observations are based on Tropical Rainfall Measuring
144 Mission (TRMM, version 3B42; Huffman et al. 1995). The raw 3-hourly TRMM rainfall with a
145 0.25-degree spatial resolution was interpolated onto $1^o \times 1^o$ daily data. Daily atmospheric fields
146 including 3D winds, relative humidity, temperature, and SST during the same period from the
147 recent ECMWF ERA-Interim reanalysis (Dee et al. 2011) with a horizontal resolution of 1.5°×1.5°,
148 are also analyzed. In this study, our analysis will focus on TCs exceeding tropical storm strength in
149 both observations and HiRAM simulations

150 Following Jiang et al. (2011), extended empirical orthogonal function (EEOF) analyses
151 (Weare and Nasstrom 1982) of daily 10-90-day band-pass filtered rainfall anomalies over the
152 EPAC (140°W–90°W; EQ-30°N) from 1998-2008 are performed to define the leading ISV modes
153 in both observations and simulations. Temporal lags of 21 days are adopted for EEOF analyses.
154 Similar to EEOF results as presented in Jiang et al. (2011), the first two leading EEOF modes of
155 both observed and simulated daily rainfall anomalies capture the dominant 40-day ISV modes
156 associated with the EPAC ITCZ. Then these two leading principal components (PCs), which are in
157 quadrature with each other, are used to determine daily ISV amplitudes and phases (ranging from 1
158 to 8, then back to phase 1) following a similar method employed in Wheeler and Hendon (2004) for
159 the MJO. Composite analysis for observed and simulated rainfall can then be accomplished by
160 averaging the band-pass filtered rainfall anomalies over each ISV phase based on selected strong
161 ISV events ($\sqrt{PC_1^2 + PC_2^2} \geq 1.0$) during the EPAC hurricane season (June-October) from 1998-2008.

162 It is noteworthy that rainfall associated with TCs may contribute to ISV variances as
163 illustrated by a study over the western Pacific (Hsu et al. 2008). Sensitivity tests are thus conducted
164 by conducting EOF analyses of the same 10-90-day band-pass filtered TRMM rainfall dataset to

affirm that the dominant ISV modes over the EPAC derived by the EEOF approach are independent from TC activity. The first two leading EOF modes of observed rainfall anomalies during May-October of 1998-2008 (e.g., total 2024 days) capture similar ISV patterns as depicted by the two leading EEOF modes; the two quadratic patterns of EOF_1 and EOF_2 modes represent anomalous rainfall patterns at phase 8 and phase 2 derived by the two leading EEOF modes, respectively (figure not shown). An additional EOF analysis of TRMM rainfall is then conducted by excluding any day during the 11 summers when a TC was reported anywhere over the EPAC. Results show that the two leading EOF modes of rainfall anomalies during these non-TC days (total 1106 days) are largely identical to those based on rainfall during the full period of the 11 summers. Therefore, the 40-day ISV mode over the EPAC as extracted by EEOF or EOF analysis represents an intrinsic regional low-frequency convective variability mode independent from TC activities. Since the EEOF approach exerts stronger constraints to the derived dominant ISV modes than the EOF analysis by providing temporal evolution of the spatial patterns associated with the leading ISV modes, we employ the PCs corresponding to the two leading EEOFs to define the daily phases of the 40-day ISV mode over the EPAC.

3. Modulations of the ISV on TC activity in GCM simulations

Left panels (a-d) in Figure 1 illustrate observed rainfall anomalies (shaded) along with TC genesis locations from 1998-2008 during a life cycle of the ISV. As previously documented (Jiang and Waliser 2008; Maloney et al. 2008), the EPAC ISV exhibits both eastward and northward propagation. In agreement with previous studies (e.g., Maloney and Hartmann 2000b), strong modulations of TC genesis over the EPAC by the ISV is clearly observed. TC genesis largely occurs over regions with enhanced ISV convection. The northward migration of the TC genesis zone from phases 6+7 (Fig. 1d) to phases 1+8 (Fig. 1a), and then to phases 2+3 (Fig. 1b), coupled with the northward movement of enhanced ISV convection is clearly evident. The largely suppressed ISV convection over the EPAC during phases 4+5 is also consistent with significantly

reduced TC genesis at this time. It is also noteworthy that a clear poleward shift of the TC genesis belt relative to maximum ISV convection is discerned for ISV phases 6+7 (Fig. 1d).

An identical analysis to that performed on the observations was carried out on the HiRAM output. The bulk features of rainfall anomalies associated with the observed ISV over the EPAC are captured well in the HiRAM simulations (shaded; Figs. 1e-h), which have been comprehensively examined in Jiang et al. (2011). Of particular interest is that strong modulation of TC genesis by the model ISV, as exhibited in the observations, is depicted well in HiRAM, including the northward migration of TC genesis belt from phases 6+7 to phases 2+3, and the considerably smaller TC genesis during phases 4+5. In addition, the poleward shift of TC genesis relative to the convection maximum is also noted in model simulations during phases 6+7 (Fig. 1h), although most model TC genesis favors longitudes east of 120^{o}W, while genesis is still evident west of 120^{o}W in the observations (Fig. 1d). This could be associated with the eastward displacement of the maximum convection center in HiRAM simulations (Fig. 1h) relative to its observed counterpart (Fig. 1d).

Figure 2 further illustrates strong impacts of the ISV on TC genesis by displaying TC genesis counts over the EPAC during each ISV phase from 1 to 8, as well as during a weak ISV period as denoted by ISV phase "0" with gray bars in both the observation and HiRAM simulation plots. Again it is clearly illustrated (Fig. 2a) that many more TCs form during ISV phases 1, 7, and 8, with only a few cases occurring during phases 4-6. A relatively small number of TCs originate during weak ISV phases. HiRAM captures the observed variation of TC counts as a function of ISV phase very well (Fig. 2b).

To demonstrate how ISV modulates TC movements, in addition to TC genesis locations (i.e., Fig. 1), six-hourly TC positions during each ISV phase are plotted in Fig. 3 for both observations and simulations. Again, significant impacts of the ISV on TC movements over the EPAC as seen in the observations are well captured in HiRAM. In both observations and model simulations, TCs largely cluster over regions with enhanced ISV convection, while TC activity is greatly reduced

over regions with suppressed ISV convection. Consistent with the previous discussion, TC activity exhibits a slight northward shift relative to active ISV convection near 10°N during phases 6+7, in both observations (Fig. 3d) and simulations (Fig. 3h).

4. Factors controlling the intraseasonal TC activity over the EPAC

In this section, we explore key factors associated with the ISV in modulating TC genesis over the EPAC by utilizing an empirical genesis potential index (GPI; Emanuel and Nolan 2004), which is defined as follows,

$$GPI = \underbrace{\left|10^5\zeta\right|^{3/2}}_{\eta}\ \underbrace{\left(\frac{\gamma}{50}\right)^3}_{r}\ \underbrace{\left(\frac{\mathrm{PI}}{70}\right)^3}_{\psi}\ \underbrace{\left(1+0.1\cdot V_{Shear}\right)^{-2}}_{s} \qquad (1)$$

where ζ is the 850hPa absolute vorticity (s^{-1}), γ is the relative humidity at 600hPa (%), PI is the potential intensity in terms of wind speed (ms^{-1}), which gives an upper bound on TC intensity (Bister and Emanuel 2002); and V_{shear} is the magnitude of the vertical wind shear between 850 and 200hPa (ms^{-1}). Terms η, r, ψ, and s denote the GPI components associated with 850hPa absolute vorticity, 600hPa relative humidity, potential intensity, and vertical wind shear, respectively.

It has been illustrated that the GPI is able to replicate the observed climatological annual cycle as well as interannual variations of TC genesis in several different basins (Camargo et al. 2007a). On intraseasonal time scales, the GPI also exhibits capability in representing global TC genesis (Camargo et al. 2009; hereafter CWS09). Based on an analysis of budget terms of anomalous GPI, CWS09 further examined the roles of the four environmental variables in Eq. (1) associated with the MJO in modulating TC genesis over the global oceans. It is suggested that mid-level humidity plays a leading role in the MJO modulation of TC genesis frequency, with a secondary role for the vorticity and a very weak influence of vertical shear and potential intensity. This differs from results from previous studies (Maloney and Hartmann 2000b, a; Hall et al. 2001; Bessafi and Wheeler 2006) that pointed to the dynamical factors, including low-level vorticity and vertical wind shear, as being most relevant for the MJO modulation of TCs. Also in CWS09, the first-position

density field was used to represent TC genesis frequency with nine grid points smoothing, which makes it difficult to characterize detailed features of TC genesis over a small ocean basin such as the EPAC. Here, we analyze the actual TC genesis location during ISV phases. Also the new ERA-Interim reanalysis with improved quality and horizontal resolution is employed for the calculation of daily GPI patterns. Moreover, GPI anomalies associated with the ISV are also calculated based on HiRAM simulations, which may provide further indications of physics regulating TC genesis in the observations.

Figures 4a-d show evolution of anomalous GPI (shaded) along with TC genesis during ISV phases based on observations. Observed rainfall anomalies in each phase as displayed in Figs. 1a-d are duplicated with green contours. It is shown that positive (negative) GPI anomalies are generally collocated with enhanced (suppressed) convection. The majority of TC genesis occurs over positive anomalous GPI regions. Particularly noteworthy is the poleward shift of a positive GPI pattern relative to enhanced convection during phases 6+7 (Fig. 4d). TC genesis during this period is well depicted by positive GPI anomalies rather than convection itself as discussed in Fig. 1. A small number of TCs are also observed over negative GPI regions, e.g., during phases 4+5, which could be ascribed to factors that are not included in Eq. (1) or not associated with the 40-day ISV mode discussed here (e.g., quasi-biweekly ISV mode, or smaller scale convectively coupled waves and easterly waves).

The evolution of anomalous GPI patterns along with rainfall anomalies and TC genesis during different ISV phases in HiRAM simulations is displayed in Figs. 4e-h. While simulated GPI anomalies exhibit slightly weaker amplitudes than their observed counterparts, model TC genesis also largely occurs over regions with positive GPI anomalies as in the observations. Of particular interest is that the poleward displacement of positive GPI relative to maximum convection during phases 6+7 as previously noted in the observations is also clearly evident in HiRAM simulations (Fig. 4h). Also in agreement with the observations, positive GPI anomalies show better consistency with model TC genesis than convection anomalies.

Since the anomalous GPI patterns generally represent TC genesis during ISV evolution very well in both observations and simulations, we proceed to assess the relative roles of the four elements in Eq. (1) in contributing to total GPI anomalies. For clarification purposes, any variable A can be decomposed into a climatological annual cycle component ($\overline{A}$) and a departure from climate component (A'), which contains variability on various time scales from synoptic, to intraseasonal, and to interannual time scales; i.e., $A = \overline{A} + A'$, where A represents each GPI component in Eq. (1), η, r, ψ, and s. Then the anomalous GPI associated with the ISV (GPI^{isv}) can be written as follows,

$$GPI^{isv} = \bar{r}\,\overline{\psi s}\,\eta^{isv} + \bar{\eta}\,\overline{\psi s} r^{isv} + \overline{\eta r s}\,\psi^{isv} + \overline{\eta r}\,\overline{\psi} s^{isv} + \{\overline{\psi s}(r'\eta')^{isv} + \bar{r}\,\overline{\psi}(s'\eta')^{isv} + \ldots + \overline{\psi}(s'r'\eta')^{isv} + \ldots + (\eta' r'\psi' s')^{isv}\} \quad (2)$$

Similar to CWS09, the total GPI anomalies associated with the ISV can be decomposed into four linear terms which are associated with the ISV of each of the four variables while the other three terms are kept at their summer mean values (i.e., first four terms on the r.h.s. of Eq. 2). Moreover, nonlinear effects can also be evaluated by terms which include high-order variances of two or more terms of the four variables (total 11 terms included in brackets in Eq. 2). The results suggest that contributions by ISV potential intensity to the total GPI anomalies, i.e., $\overline{\eta r s}\,\psi^{isv}$ in Eq. (2), are relatively smaller than those from the ISV of the other three variables in both observations and HiRAM simulations (to be shown in Figs. 6 and 8). Figure 5 displays observed anomalous 850hPa vorticity and winds, 600hPa relative humidity, and V_{shear} during different ISV phases along with total GPI anomalies (shaded, duplicated from Figs. 4a-d). It is shown that positive (negative) 850hPa vorticity patterns associated with the anomalous winds induced by ISV convection are in good agreement with positive (negative) GPI anomalies during each ISV phase, suggesting the important role of low-level vorticity in regulating TC genesis. Meanwhile, enhanced mid-level moisture is also found to be conducive for active TC genesis over the coastal regions off Central America during ISV phases 1+8 and 2+3 (Figs. 5e-f). An east-west dipole in 600hPa moisture anomalies is evident during phases 6+7 (Fig. 5h). While positive moisture anomalies to the west of 120^{o}W tends to sustain local positive GPI anomalies between 10-15^{o}N, negative anomalies to the

east of 120°W counteract observed positive GPI anomalies. The maximum V_{shear} anomalies over the far EPAC are largely confined south of 15°N. During phases 6+7, reduced vertical shear to the east of 120°W (Fig. 5l), largely due to weakening of low-level mean westerly flow by the northeasterly anomalous winds (Fig. 5d), contributes to locally positive GPI anomalies.

Figure 6 displays budget terms of the total anomalous GPI in Eq. (2) over three selected regions where active TC genesis is observed (see green boxes in Fig. 5). As mentioned above, the ISV of potential intensity plays a relatively minor role in contributing to total GPI anomalies over all three regions. Over the northern box region off Central America coast (110-95°W; 13-18°N), positive GPI anomalies during ISV phases 1-2 are dominated by two major terms, e.g., 850hPa vorticity and 600hPa relative humidity. For the region of 140-120°W and 10-15°N, while both 850hPa vorticity and 600hPa moisture are again the two most important terms in contributing to maximum positive GPI anomalies during phases 6-7, nonlinear terms also make comparable contributions particularly in phase 6. And for the third region of 115-95°W and 9-13°N, in addition to the contribution by 850hPa vorticity, the major contribution to the maximum positive GPI during phases 6-7 is by the reduced vertical wind shear; mid-level humidity associated with the ISV tends to reduce the total GPI anomalies in phase 6. Meanwhile, contributions from nonlinear terms are also noted over this region.

Further analyses illustrate that the nonlinear contributions to observed GPI anomalies associated with the 40-day ISV mode during phases 6-7 over the two box regions near 10°N (Figs. 6b and 6c) are largely due to covariance terms of 850hPa vorticity and mid-level humidity anomalies (i.e., $\overline{\psi' s}(r'\eta')^{isv}$ in Eq. 2) on both synoptic (< 8days) and high-frequency ISV scales (8-20 days). While further studies are needed to explore physics responsible for this upscale contribution to the GPI anomalies associated with the 40-day ISV mode, this result is largely in concert with vigorous activity of easterly waves and the quasi-biweekly ISV mode observed over the fast EPAC near 10°N during boreal summer (e.g., Serra et al. 2010; Jiang and Waliser 2009).

The above results suggest that the poleward shift of TC genesis relative to maximum ISV convection observed in ISV phases 6+7 (Fig. 1d) are largely due to the presence of positive low-level vorticity, enhanced mid-level moisture, and reduced vertical wind shear to the north of convection (cf. Figs. 4d, 5d, 5h, and 5l). The northward shift of positive vorticity relative to ISV convection could result from the coupling between ISV convection and summer mean monsoonal flow with an easterly vertical shear (Jiang et al. 2004; Jiang and Waliser 2008). As the maximum amplitude of easterly vertical wind shear over the EPAC is present near 8^{o}N (Jiang and Waliser 2008), this may explain why the strongest northward displacement of GPI anomalies relative to the convection is observed during phases 6+7 when enhanced convection is largely confined south of 10^{o}N (Fig. 4d). While a northward shift of lower tropospheric specific humidity anomalies to ISV convection has been illustrated on a pressure-latitude plane in Jiang and Waliser (2008), further analysis is warranted for better understanding of 3D anomalous relative humidity pattern associated with the EPAC ISV.

To further understand physics in regulating TC genesis in HiRAM, we proceed to examine roles of the four GPI factors for total simulated GPI anomalies. Figure 7 displays similar anomalous 850hPa vorticity and winds, 600hPa relative humidity, and V_{shear} during different ISV phases along with total GPI anomalies as in Fig. 5 but based on HiRAM simulations. In general, similar evolutionary features in these anomalous fields associated with the ISV as in the observations are noted in simulations. Positive 850hPa vorticity is in accord with positive GPI anomalies during the ISV evolution (Figs.7a-d), again suggesting the importance of low-level vorticity in modulating TC genesis in HiRAM. Consistency between enhanced mid-level relative humidity and positive GPI anomalies over the coastal region off Central America during phases 1+8 and phases 2+3 (Figs. 7e-f) is also discerned in model simulations. Meanwhile, enhanced (reduced) vertical wind shear during ISV phases 1+8 and 2+3 (phases 4+5 and 6+7) over the far EPAC is also generally consistent with observations, though model deficiencies in anomalous humidity and wind shear patterns are also noticed. A positive moisture center during phases 6+7 is found near 112^{o}W, 8^{o}N in

GCM (Fig. 7h); instead, the observed positive relative humidity center is located near 135^{o}W, 17^{o}N during this period (Fig. 5h). Since this positive 600hPa relative humidity plays an active role in contributing the observed positive GPI over the western part of the EPAC along 10^{o}N during phases 6+7 (see Figs. 5h and 6b), the model biases in simulating 600hPa moisture anomalies may partially explain the less elongated positive GPI band during phases 6+7 in HiRAM, leaving the model TC genesis largely confined to the eastern part of the EPAC rather than more wide-spread along 10^{o}N in the observations. Moreover, the amplitude of reduced vertical wind shear during phases 6+7 in HiRAM is much weaker than its observational counterpart (c.f., Figs. 5l and 7l), which could lead to the weaker positive GPI anomalies during phases 6+7 in HiRAM than in the observations.

Figure 8 further displays budget terms of total GPI anomalies based on model simulations over two of the three rectangle regions previously shown for observations. (Due to rather weak GPI anomalies over the region of 140-120^{o}W, 10-15^{o}N in HiRAM, model results are not displayed for this region). It is shown that the role of potential intensity associated with the ISV for total simulated GPI anomalies is negligible throughout the life cycle of ISV over both of the two box regions. This could be largely ascribed to the lack of the ISV in the SST fields in the GCM as monthly mean SSTs have been specified in these AMIP-type integrations. For the northern box region (110-95^{o}W; 13-18^{o}N), similarly as in the observations, both low-level vorticity and mid-level relative humidity play comparable roles for total GPI anomalies in the GCM. For the southern region along 10^{o}N (115-95^{o}E; 9-13^{o}N), the predominant role of reduced vertical shear for the total GPI anomalies during phase 6 in the observations is not evident in HiRAM (c.f., Figs. 6c and 8b); instead, low-level vorticity takes a leading role in contributing total GPI anomalies in HiRAM, which again could be due to the aforementioned weaker amplitude of reduced vertical wind shear during this period in the GCM. Moreover, simulated total GPI anomalies in phase 7 are dominated by low-level vorticity and mid-level specific humidity. The role of nonlinear effects for total GPI anomalies during this period as noted in the observations is not evident in simulations. As previously discussed, the nonlinear effects for the observed GPI anomalies along 10^{o}N are closely

associated with synoptic-scale wave activity, which could be rather challenging to be well resolved by a GCM at 50km horizontal resolution. It remains an intriguing topic for future study to see how the representation of these multi-scale interactive processes can be improved in a GCM with increased horizontal resolutions.

5. Summary and discussion

In the present study, we illustrate that the observed modulations of TC genesis over the EPAC by the ISV can be faithfully represented in the GFDL HiRAM with a horizontal resolution of about 50km. This is a remarkable achievement for a climate simulation model (i.e., one that is not initialized from observations) to be capable of depicting the ISV, TC activity, as well as the intimate ISV-TC relationships. Considering the typical predictability of 2-3 weeks for ISV, these results thus suggest great potential for dynamical intraseasonal TC forecasts based on HiRAM.

Further analysis indicates that anomalous GPI patterns associated with the EPAC ISV can generally well depict the modulation of TC genesis during different phases of the ISV in both observations and model simulations. Further investigation based on observations is performed to examine the key factors associated with the ISV in modulating TC activity by examining the budget terms of the total GPI anomalies during the ISV life cycle. While Camargo et al. (2009) suggested that mid-level humidity and low-level vorticity are the two most important contributors to the MJO composite GPI anomalies based on a similar analysis for global oceans, the present study based on the EPAC suggests that roles of several factors could be location- as well as ISV phase-dependent. Both the low-level vorticity and mid-level humidity play major roles for observed active TC genesis over northern EPAC warm pool during ISV phases 1+8, and to the west of 120^{o}W between 10-15^{o}N during phases 6+7. Reduced vertical wind shear and the 850hPa vorticity are the two most important factors in modulating TC genesis to the east of 120^{o}W between 10-15^{o}N during ISV phases 6+7. Nonlinear terms are also found to play more active roles over the 10-15^{o}N zone.

While in general the observed anomalous patterns of low-level vorticity, mid-level relative humidity and vertical wind shear associated with the EPAC ISV are well represented in HiRAM,

model deficiencies are also noted in simulating the anomalous mid-level relative humidity patterns and amplitude of vertical wind shear associated with the EPAC ISV, particularly during ISV phases 6+7. These model biases could be responsible for the eastward shift of model TC genesis during this period.

Acknowledgments*:* XJ acknowledges support by NOAA MAPP program under Awards NA09OAR4310191 and NA11OAR4310086, and NSF Climate and Large-Scale Dynamics under Award ATM-0934285. DW acknowledges support by U.S. Office of Naval Research under Grant (N00014-10-1-0541) through UCSD, and by NOAA CTB Program through U. HI. We thank the editor, Dr. K. Walsh, and anonymous reviewers for their constructive comments on an earlier version of this manuscript, and B. Kahn and I.-S. Kang for insightful discussions. Thanks also to T. Kubar for his comments and editorial assistance. The Fortran code for GPI calculation was obtained from K. Emanuel's website. Part of this research was carried out at the Jet Propulsion Laboratory, California Institute of Technology, under a contract with the National Aeronautics and Space Administration.

References

Aiyyer, A. and J. Molinari, 2008: MJO and Tropical Cyclogenesis in the Gulf of Mexico and Eastern Pacific: Case Study and Idealized Numerical Modeling. *J. Atmos. Sci.*, **65,** 2691-2704.

Barrett, B. S. and L. M. Leslie, 2009: Links between Tropical Cyclone Activity and Madden-Julian Oscillation Phase in the North Atlantic and Northeast Pacific Basins. *Mon. Weather Rev.*, **137**, doi:10.1175/2008MWR2602.1**,** 727-744.

Bechtold, P., M. Kohler, T. Jung, F. Doblas-Reyes, M. Leutbecher, M. J. Rodwell, F. Vitart, and G. Balsamo, 2008: Advances in simulating atmospheric variability with the ECMWF model: From synoptic to decadal time-scales. *Quart. J. Roy. Meteor. Soc.*, **134**, Doi 10.1002/Qj.289**,** 1337-1351.

Belanger, J. I., J. A. Curry, and P. J. Webster, 2010: Predictability of North Atlantic Tropical Cyclone Activity on Intraseasonal Time Scales. *Mon. Weather Rev.*, **138**, 10.1175/2010mwr3460.1**,** 4362-4374.

Bessafi, M. and M. C. Wheeler, 2006: Modulation of south Indian ocean tropical cyclones by the Madden-Julian oscillation and convectively coupled equatorial waves. *Mon. Weather Rev.*, **134,** 638-656.

Bister, M. and K. A. Emanuel, 2002: Low frequency variability of tropical cyclone potential intensity - 1. Interannual to interdecadal variability. *J. Geophys. Res.*, **107**, 10.1029/2001JD000776.

Camargo, S. J., K. A. Emanuel, and A. H. Sobel, 2007a: Use of a Genesis Potential Index to Diagnose ENSO Effects on Tropical Cyclone Genesis. *J. Clim.*, **20**, doi:10.1175/JCLI4282.1**,** 4819-4834.

Camargo, S. J., M. C. Wheeler, and A. H. Sobel, 2009: Diagnosis of the MJO Modulation of Tropical Cyclogenesis Using an Empirical Index. *J. Atmos. Sci.*, **66**, Doi 10.1175/2009jas3101.1**,** 3061-3074.

Camargo, S. J., A. W. Robertson, S. J. Gaffney, P. Smyth, and M. Ghil, 2007b: Cluster analysis of typhoon tracks. Part I: General properties. *J. Clim.*, **20**, 10.1175/JCLI4188.1**,** 3635-3653.

de Szoeke, S. P. and C. S. Bretherton, 2005: Variability in the southerly flow into the eastern Pacific ITCZ. *J. Atmos. Sci.*, **62,** 4400-4411.

Dee, D. P., et al., 2011: The ERA-Interim reanalysis: configuration and performance of the data assimilation system. *Quart. J. Roy. Meteor. Soc.*, **137**, 10.1002/qj.828**,** 553-597.

Elsberry, R. L., M. S. Jordan, and F. Vitart, 2010: Predictability of tropical cyclone events on intraseasonal timescale with the ECMWF monthly forecast model. *Asia-Pacific J. Atmos. Sci.*, **46,** 135-153.

Emanuel, K. A. and D. S. Nolan, 2004: Tropical cyclone activity and global climate. *Preprints, 26th Conf. on Hurricanes and Tropical Meteorology*, Amer. Meteor. Soc., Miami, FL, 240-241.

Frank, W. M. and P. E. Roundy, 2006: The role of tropical waves in tropical cyclogenesis. *Mon. Weather Rev.*, **134,** 2397-2417.

Goldenberg, S. B. and L. J. Shapiro, 1996: Physical Mechanisms for the Association of El Niño and West African Rainfall with Atlantic Major Hurricane Activity. *J. Clim.*, **9**, 10.1175/1520-0442**,** 1169-1187.

Gray, W. M., 1984: Atlantic seasonal hurricane frequency I: El-Nino and 30mb Quasi-Biennial Oscillation influences. *Mon. Weather Rev.*, **112,** 1649-1668.

Hall, J. D., A. J. Matthews, and D. J. Karoly, 2001: The modulation of tropical cyclone activity in the Australian region by the Madden-Julian oscillation. *Mon. Weather Rev.*, **129,** 2970-2982.

Held, I. M. and M. Zhao, 2011: The response of tropical cyclone statistics to an increase in CO2 with fixed sea surface temperatures. *J. Clim.*, 10.1175/jcli-d-11-00050.1.

Higgins, R. W. and W. Shi, 2001: Intercomparison of the Principal Modes of Interannual and Intraseasonal Variability of the North American Monsoon System. *J. Clim.*, **14,** 403-417.

Ho, C. H., J. H. Kim, J. H. Jeong, H. S. Kim, and D. L. Chen, 2006: Variation of tropical cyclone activity in the South Indian Ocean: El Nino-Southern Oscillation and Madden-Julian Oscillation effects. *J. Geophys. Res.*, **111**, 10.1029/2006JD007289.

Hsu, H.-H., C.-H. Hung, A.-K. Lo, C.-C. Wu, and C.-W. Hung, 2008: Influence of Tropical Cyclones on the Estimation of Climate Variability in the Tropical Western North Pacific. *J. Clim.*, **21**, 10.1175/2007jcli1847.1**,** 2960-2975.

Huffman, G. J., R. F. Adler, B. Rudolf, U. Schneider, and P. R. Keehn, 1995: Global Precipitation Estimates Based on a Technique for Combining Satellite-Based Estimates, Rain-Gauge Analysis, and Nwp Model Precipitation Information. *J. Clim.*, **8,** 1284-1295.

Jarvinen, B. R., C. J. Neumann, and M. A. S. Davis, 1984: A tropical cyclone data tape for the North Atlantic Basin, 1886-1983: Contents, limitations, and uses. NOAA Tech. Memo. NWS NHC 22, 21pp.

476 Jiang, X. and D. E. Waliser, 2008: Northward propagation of the subseasonal variability over the
477 eastern Pacific warm pool. *Geophys. Res. Lett.*, **35**, L09814, doi:10.1029/2008GL033723.
478 ——, 2009: Two dominant subseasonal variability modes of the eastern Pacific ITCZ. *Geophys.*
479 *Res. Lett.*, **36**, L04704, doi: 10.1029/2008gl036820.
480 Jiang, X., T. Li, and B. Wang, 2004: Structures and Mechanisms of the Northward Propagating
481 Boreal Summer Intraseasonal Oscillation. *J. Clim.*, **17,** 1022-1039.
482 Jiang, X., D. E. Waliser, M. C. Wheeler, C. Jones, M. N. Lee, and S. D. Schuert, 2008: Assessing
483 the skill of an all-season statistical forecast model for the Madden-Julian oscillation. *Mon.*
484 *Weather Rev.*, **136**, DOI:10.1175/2007MWR2305.1**,** 1940-1956.
485 Jiang, X., D. Waliser, D. Kim, M. Zhao, K. Sperber, W. Stern, S. Schubert, G. Zhang, W. Wang, M.
486 Khairoutdinov, R. Neale, and M.-I. Lee, 2011: Simulation of the intraseasonal variability over
487 the Eastern Pacific ITCZ in climate models. *Climate Dyn.*, 10.1007/s00382-011-1098-x**,** 1-20.
488 Kayano, M. T. and V. E. Kousky, 1999: Intraseasonal (30-60 day) variability in the global tropics:
489 principal modes and their evolution. *Tellus Series a-Dynamic Meteorology and*
490 *Oceanography*, **51,** 373-386.
491 Kikuchi, K. and B. Wang, 2010: Formation of Tropical Cyclones in the Northern Indian Ocean
492 Associated with Two Types of Tropical Intraseasonal Oscillation Modes. *J. Meteorol. Soc.*
493 *Japan*, **88,** 475-496.
494 Kim, D., et al., 2009: Application of MJO Simulation Diagnostics to Climate Models. *J. Clim.*, **22**,
495 Doi 10.1175/2009jcli3063.1**,** 6413-6436.
496 Klotzbach, P. J., 2010: On the Madden-Julian Oscillation-Atlantic Hurricane Relationship. *J. Clim.*,
497 **23**, doi:10.1175/2009JCLI2978.1**,** 282-293.
498 Knutson, T. R. and K. M. Weickmann, 1987: 30-60 Day Atmospheric Oscillations: Composite Life
499 Cycles of Convection and Circulation Anomalies. *Mon. Weather Rev.*, **115,** 1407-1436.
500 Lau, W. K.-M. and D. E. Waliser, 2011: *Intraseasonal Variability in the Atmosphere-Ocean*
501 *Climate System*. Second ed. Springer, in press, Heidelberg, Germany.
502 Leroy, A. and M. C. Wheeler, 2008: Statistical Prediction of Weekly Tropical Cyclone Activity in
503 the Southern Hemisphere. *Mon. Weather Rev.*, **136**, Doi 10.1175/2008mwr2426.1**,** 3637-
504 3654.
505 Liebmann, B., H. H. Hendon, and J. D. Glick, 1994: The Relationship between Tropical Cyclones
506 of the Western Pacific and Indian Oceans and the Madden-Julian Oscillation. *J. Meteorol.*
507 *Soc. Japan*, **72,** 401-412.

508 Lin, J.-L., et al., 2006: Tropical Intraseasonal Variability in 14 IPCC AR4 Climate Models. Part I:
509 Convective Signals. *J. Clim.*, **19,** 2665-2690.
510 Lorenz, D. J. and D. L. Hartmann, 2006: The Effect of the MJO on the North American Monsoon.
511 *J. Clim.*, **19,** 333-343.
512 Madden, R. A. and P. R. Julian, 1994: Observations of the 40-50-Day Tropical Oscillation: A
513 Review. *Mon. Weather Rev.*, **122,** 814-837.
514 Magana, V., J. A. Amador, and S. Medina, 1999: The midsummer drought over Mexico and Central
515 America. *J. Clim.*, **12,** 1577-1588.
516 Maloney, E. D. and D. L. Hartmann, 2000a: Modulation of hurricane activity in the Gulf of Mexico
517 by the Madden-Julian oscillation. *Science*, **287,** 2002-2004.
518 ——, 2000b: Modulation of Eastern North Pacific Hurricanes by the Madden-Julian Oscillation. *J.*
519 *Clim.*, **13,** 1451-1460.
520 Maloney, E. D. and S. K. Esbensen, 2003: The Amplification of East Pacific Madden-Julian
521 Oscillation Convection and Wind Anomalies during June-November. *J. Clim.*, **16,** 3482-3497.
522 Maloney, E. D. and S. K. Esbensen, 2007: Satellite and Buoy Observations of Boreal Summer
523 Intraseasonal Variability in the Tropical Northeast Pacific. *Mon. Weather Rev.*, **135,** 3-19.
524 Maloney, E. D. and J. Shaman, 2008: Intraseasonal Variability of the West African Monsoon and
525 Atlantic ITCZ. *J. Clim.*, **21,** 2898-2918.
526 Maloney, E. D., D. B. Chelton, and S. K. Esbensen, 2008: Subseasonal SST variability in the
527 tropical eastern north Pacific during boreal summer. *J. Clim.*, **21**, Doi
528 10.1175/2007jcli1856.1**,** 4149-4167.
529 Martin, E. R. and C. Schumacher, 2010: Modulation of Caribbean Precipitation by the Madden-
530 Julian Oscillation. *J. Clim.*, doi:10.1175/2010JCLI3773.1**,** in press.
531 Mo, K. C., 2000: The association between intraseasonal oscillations and tropical storms in the
532 Atlantic basin. *Mon. Weather Rev.*, **128,** 4097-4107.
533 Molinari, J., D. Knight, M. Dickinson, D. Vollaro, and S. Skubis, 1997: Potential vorticity, easterly
534 waves, and eastern Pacific tropical cyclogenesis. *Mon. Weather Rev.*, **125,** 2699-2708.
535 Nakazawa, T., 1988: Tropical Super Clusters within Intraseasonal Variations over the Western
536 Pacific. *J. Meteorol. Soc. Japan*, **66,** 823-839.
537 Rashid, H. A., H. H. Hendon, M. C. Wheeler, and O. Alves, 2011: Prediction of the Madden-Julian
538 oscillation with the POAMA dynamical prediction system. *Climate Dyn.*, **36**,
539 10.1007/s00382-010-0754-x**,** 649-661.

Serra, Y. L., G. N. Kiladis, and K. I. Hodges, 2010: Tracking and Mean Structure of Easterly Waves over the Intra-Americas Sea. *J. Clim.*, **23**, doi:10.1175/2010JCLI3223.1**,** 4823-4840.

Shapiro, L. J., 1987: Month-to-Month Variability of the Atlantic Tropical Circulation and Its Relationship to Tropical Storm Formation. *Mon. Weather Rev.*, **115**, 10.1175/1520-0493(1987)115<2598:mtmvot>2.0.co;2**,** 2598-2614.

Slingo, J. M., et al., 1996: Intraseasonal oscillations in 15 atmospheric general circulation models: Results from an AMIP diagnostic subproject. *Climate Dyn.*, **12,** 325-357.

Small, R. J., S. P. De Szoeke, and S.-P. Xie, 2007: The Central American midsummer drought: Regional aspects and large-scale forcing. *J. Clim.*, **20**, Doi 10.1175/Jcli4261.1**,** 4853-4873.

Vitart, F., 2009: Impact of the Madden Julian Oscillation on tropical storms and risk of landfall in the ECMWF forecast system. *Geophys. Res. Lett.*, **36**, L15802, Doi 10.1029/2009gl039089**,** -.

Vitart, F. and F. Molteni, 2010: Simulation of the Madden-Julian Oscillation and its teleconnections in the ECMWF forecast system. *Quart. J. Roy. Meteor. Soc.*, **136**, Doi 10.1002/Qj.623**,** 842-855.

Vitart, F., A. Leroy, and M. C. Wheeler, 2010: A Comparison of Dynamical and Statistical Predictions of Weekly Tropical Cyclone Activity in the Southern Hemisphere. *Mon. Weather Rev.*, **138**, Doi 10.1175/2010mwr3343.1**,** 3671-3682.

Waliser, D. E., 2006: Predictability of tropical intraseasonal variability. *Predictability of weather and climate*, T. Palmer and R. Hagedorn, Eds., Cambridge University Press718.

——, 2011: Predictability and Forecasting. *Intraseasonal Variability in the Atmosphere-Ocean Climate System*, Second ed. W. K. M. Lau and D. E. Waliser, Eds., Springer, Heidelberg, Germany, In Press.

Waliser, D. E., et al., 2003: AGCM simulations of intraseasonal variability associated with the Asian summer monsoon. *Climate Dyn.*, **21**, DOI 10.1007/s00382-003-0337-1**,** 423-446.

Wang, B. and X. Zhou, 2008: Climate variation and prediction of rapid intensification in tropical cyclones in the western North Pacific. *Meteorol. Atmos. Phys.*, **99**, 10.1007/s00703-006-0238-z**,** 1-16.

Weare, B. C. and J. S. Nasstrom, 1982: Examples of Extended Empirical Orthogonal Function Analyses. *Mon. Weather Rev.*, **110,** 481-485.

Wheeler, M. C. and H. H. Hendon, 2004: An All-Season Real-Time Multivariate MJO Index: Development of an Index for Monitoring and Prediction. *Mon. Weather Rev.*, **132,** 1917-1932.

571 Wu, M. L. C., S. D. Schubert, M. J. Suarez, and N. E. Huang, 2009: An Analysis of Moisture
572 Fluxes into the Gulf of California. *J. Clim.*, **22**, Doi 10.1175/2008jcli2525.1**,** 2216-2239.
573 Zhang, C. D., 2005: Madden-Julian oscillation. *Rev. Geophys.*, **43**, RG2003, DOI:
574 10.1029/2004RG000158**,** 36.
575 Zhang, Q. and H. v. d. Dool, 2011: Relative merit of model improvement versus availability of
576 retrospective forecasts: The case of CFS MJO prediction. *Geophys. Res. Lett.***,** submitted.
577 Zhao, M. and I. M. Held, 2010: An Analysis of the Effect of Global Warming on the Intensity of
578 Atlantic Hurricanes Using a GCM with Statistical Refinement. *J. Clim.*, **23**, Doi
579 10.1175/2010jcli3837.1**,** 6382-6393.
580 Zhao, M., I. M. Held, S. J. Lin, and G. A. Vecchi, 2009: Simulations of Global Hurricane
581 Climatology, Interannual Variability, and Response to Global Warming Using a 50-km
582 Resolution GCM. *J. Clim.*, **22**, Doi 10.1175/2009jcli3049.1**,** 6653-6678.
583

List of Figures

Figure 1 TC genesis over the EPAC from 1998-2008 during different ISV phases in the observations (left) and HiRAM simulations (right). Shading in each panel represents observed or simulated anomalous rainfall pattern with the bottom color bar for scale.

Figure 2 Counts of TC genesis over the EPAC as a function of ISV phases (phases 1 to 8 for strong ISVs while phase "0" represents weak ISV period): (a) observations and (b) HiRAM simulations. The weaker ISV is defined by amplitude of $\sqrt{PC_1^2 + PC_2^2} < 1.0$.

Figure 3 Modulation of TC movements by the EPAC ISV: (a) observations; (b) HiRAM simulations. Each mark "+" denotes the six-hourly TC location in each ISV phase in observations or GCM.

Figure 4 Composite GPI anomalies (shaded; see color scales on the right) at different ISV phases along with corresponding anomalous rainfall distributions (contours; units: mm day^{-1}) and TC genesis events based on observations (left panels) and HiRAM simulations (right panels). Solid (dashed) contours represent positive (negative) rainfall anomalies with an interval of 1 mm day^{-1}, and contours "0" are omitted.

Figure 5 (Shaded) Composite total GPI anomalies during each ISV phase (see color bar at the bottom). Left: vorticity (contours with an interval of $1.\times10^{-6}$ s^{-1}) and winds (vectors; see scale in Panel a); Middle: 600hPa relative humidity (contours with an interval of 1%); Right: 200-850hPa wind shear (contours with interval of 0.5ms^{-1}). Solid (dashed) contours denote positive (negative) values, and contours "0" are omitted in all the panels. All these above fields are based on ERA-Interim reanalysis.

Figure 6 Budget terms of the total observed GPI anomalies over three selected regions with active TC genesis (see green boxes in Figure 5) as a function of ISV phase.

Figure 7 Same as in Fig. 5 but for HiRAM simulations.

Figure 8 Same as in Fig. 6 but for HiRAM simulations over two selected regions denoted in Fig. 7e and 7l.

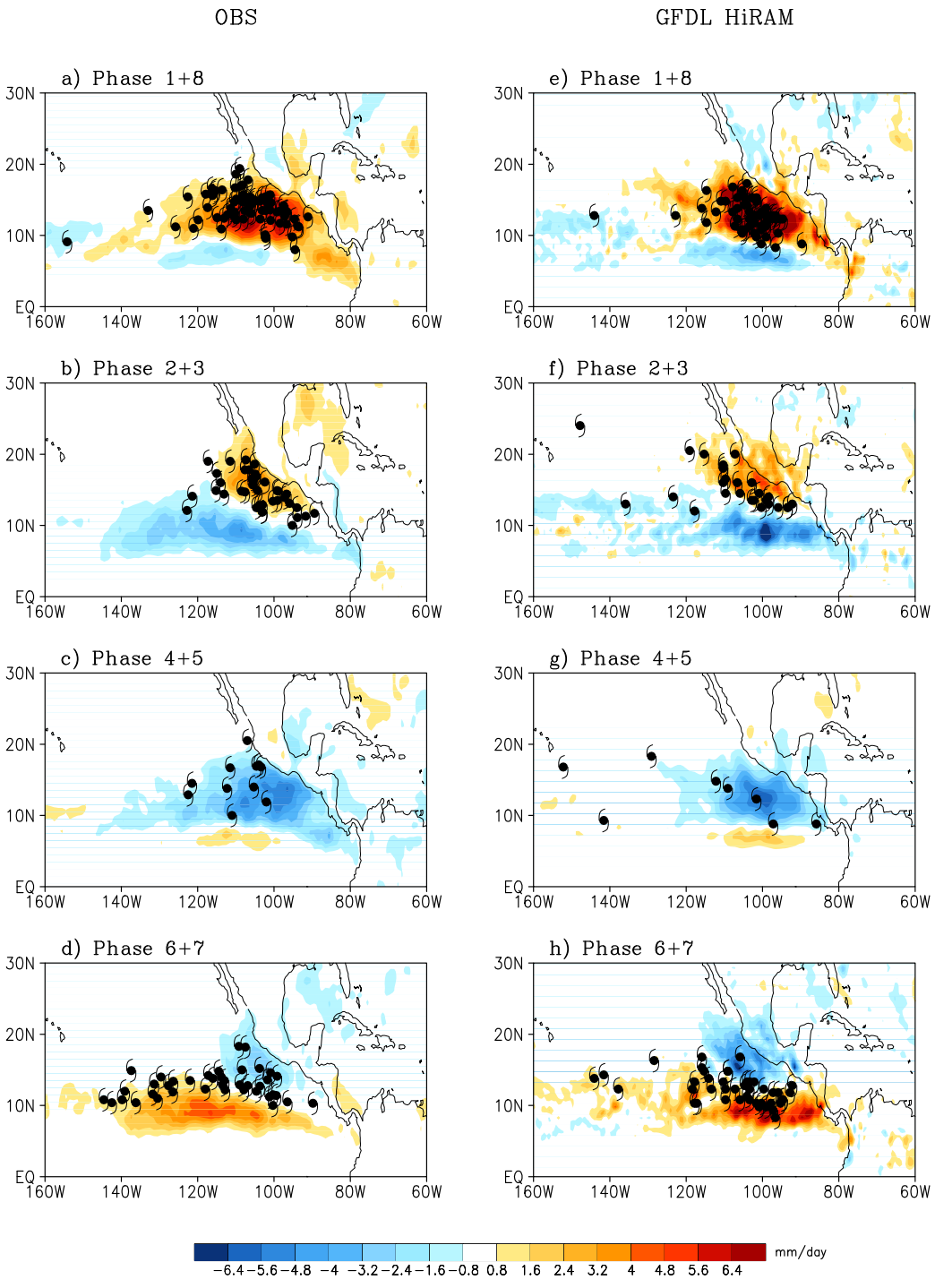

Figure 1 TC genesis over the EPAC from 1998-2008 during different ISV phases in the observations (left) and HiRAM simulations (right). Shading in each panel represents observed or simulated anomalous rainfall pattern with the bottom color bar for scale.

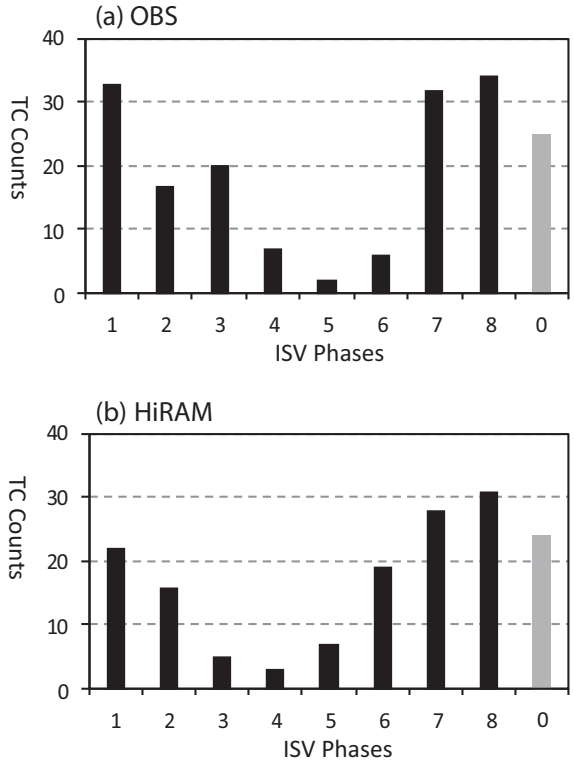

Figure 2 Counts of TC genesis over the EPAC as a function of ISV phases (phases 1 to 8 for strong ISVs while phase "0" represents weak ISV period): (a) observations and (b) HiRAM simulations. The weaker ISV is defined by amplitude of $\sqrt{PC_1^2 + PC_2^2} < 1.0$.

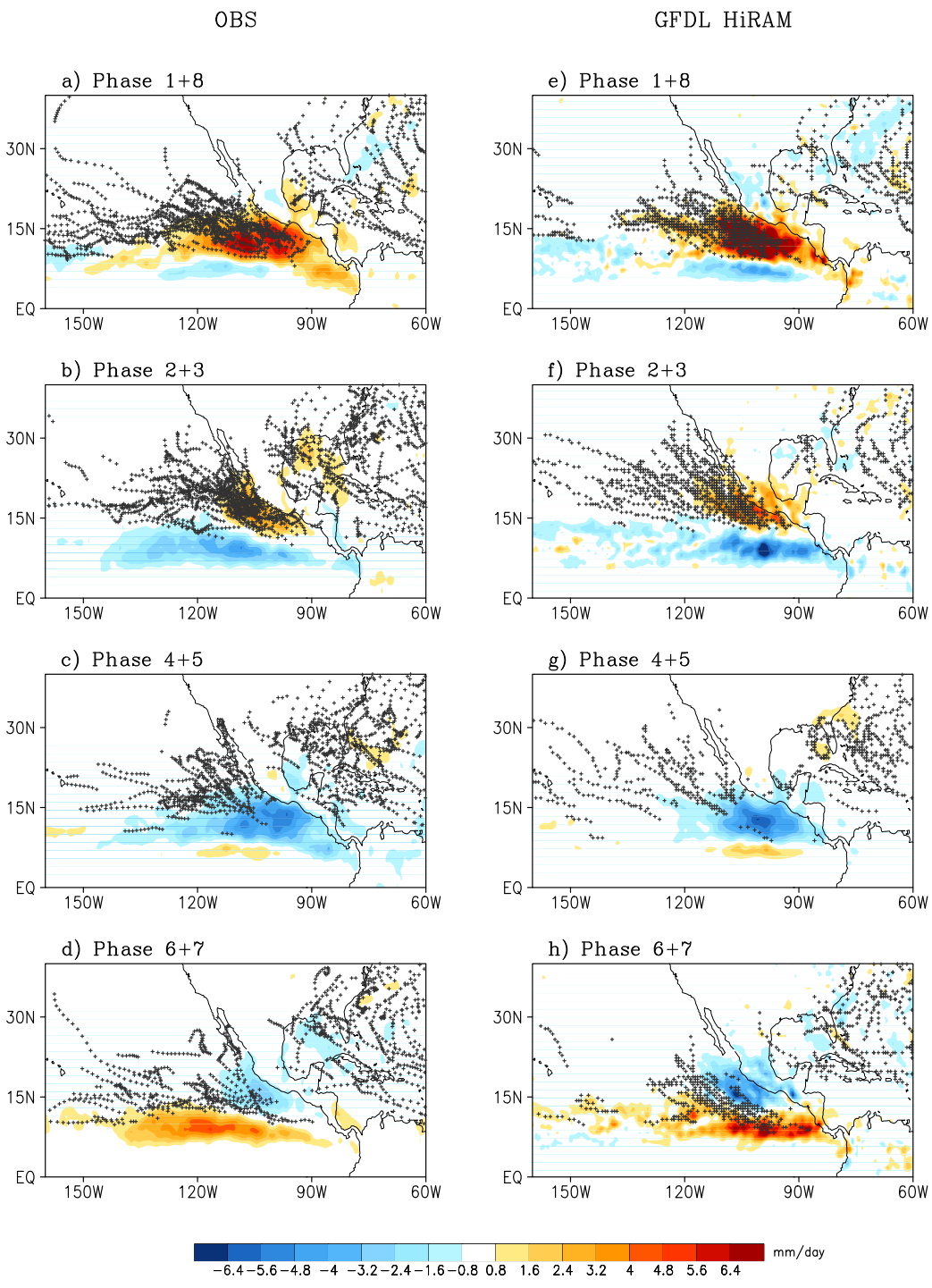

Figure 3 Modulation of TC movements by the EPAC ISV: (a) observations; (b) HiRAM simulations. Each mark "+" denotes the six-hourly TC location in each ISV phase in observations or GCM.

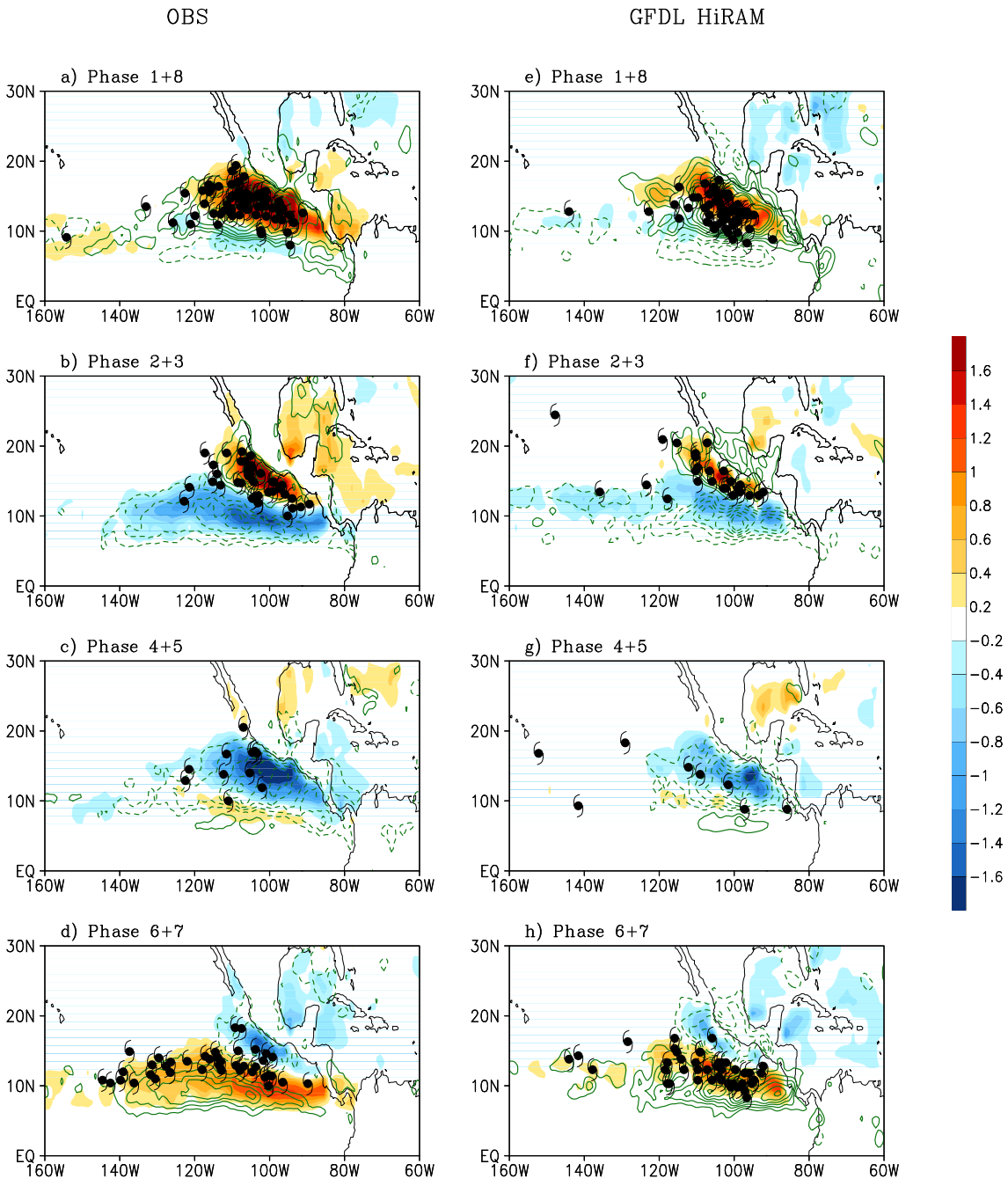

Figure 4 Composite GPI anomalies (shaded; see color scales on the right) at different ISV phases along with corresponding anomalous rainfall distributions (contours; units: mm day^{-1}) and TC genesis events based on observations (left panels) and HiRAM simulations (right panels). Solid (dashed) contours represent positive (negative) rainfall anomalies with an interval of 1 mm day^{-1}, and contours "0" are omitted.

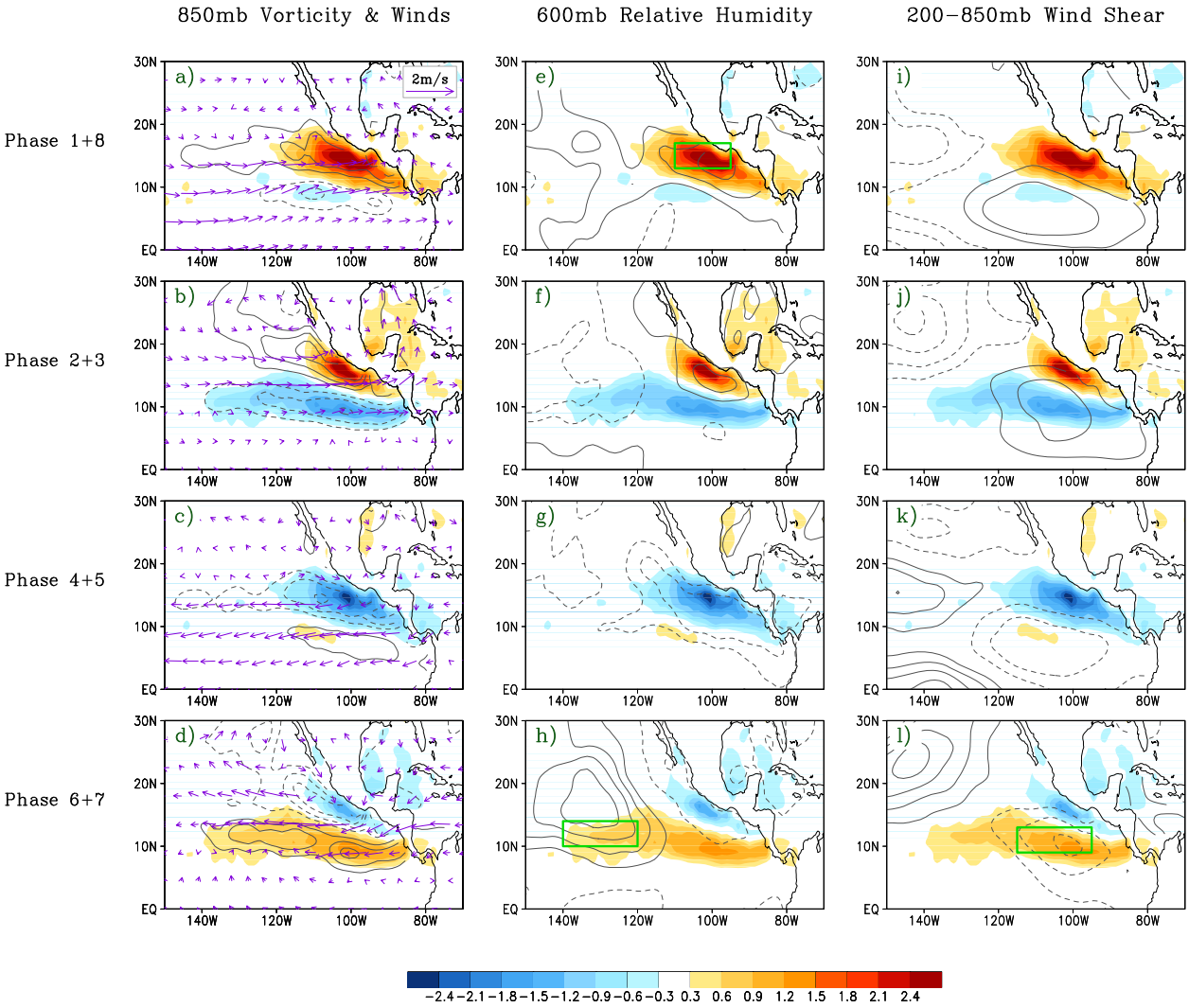

Figure 5 (Shaded) Composite total GPI anomalies during each ISV phase (see color bar at the bottom). Left: vorticity (contours with an interval of 1×10^{-6} s^{-1}) and winds (vectors; see scale in Panel a); Middle: 600hPa relative humidity (contours with an interval of 1%); Right: 200-850hPa wind shear (contours with interval of 0.5ms^{-1}). Solid (dashed) contours denote positive (negative) values, and contours "0" are omitted in all the panels. All these above fields are based on observations.

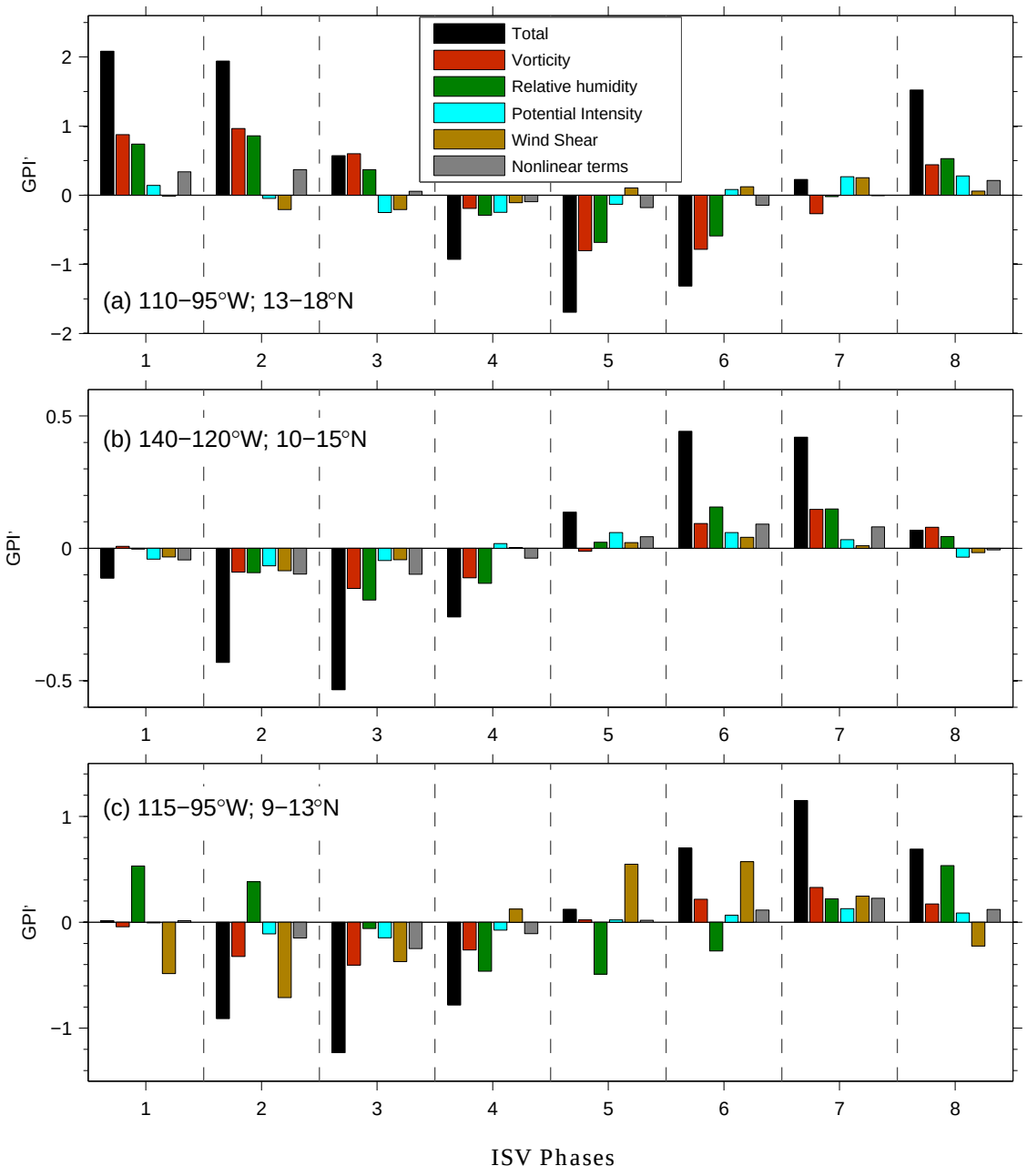

Figure 6 Budget terms of the total observed GPI anomalies over three selected regions with active TC genesis (see green boxes in Figure 5) as a function of ISV phase.

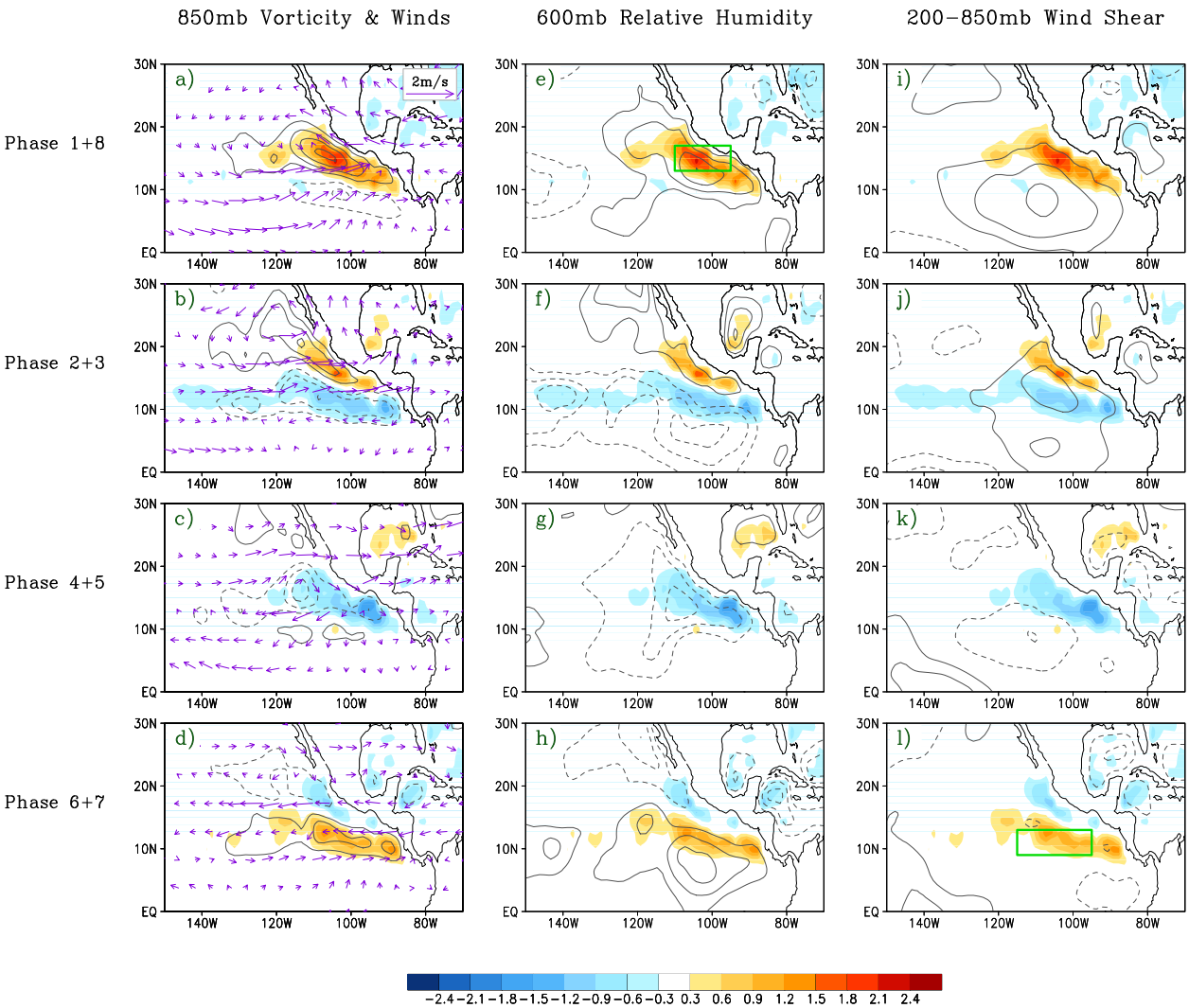

Figure 7 Same as in Fig. 5 but for HiRAM simulations.

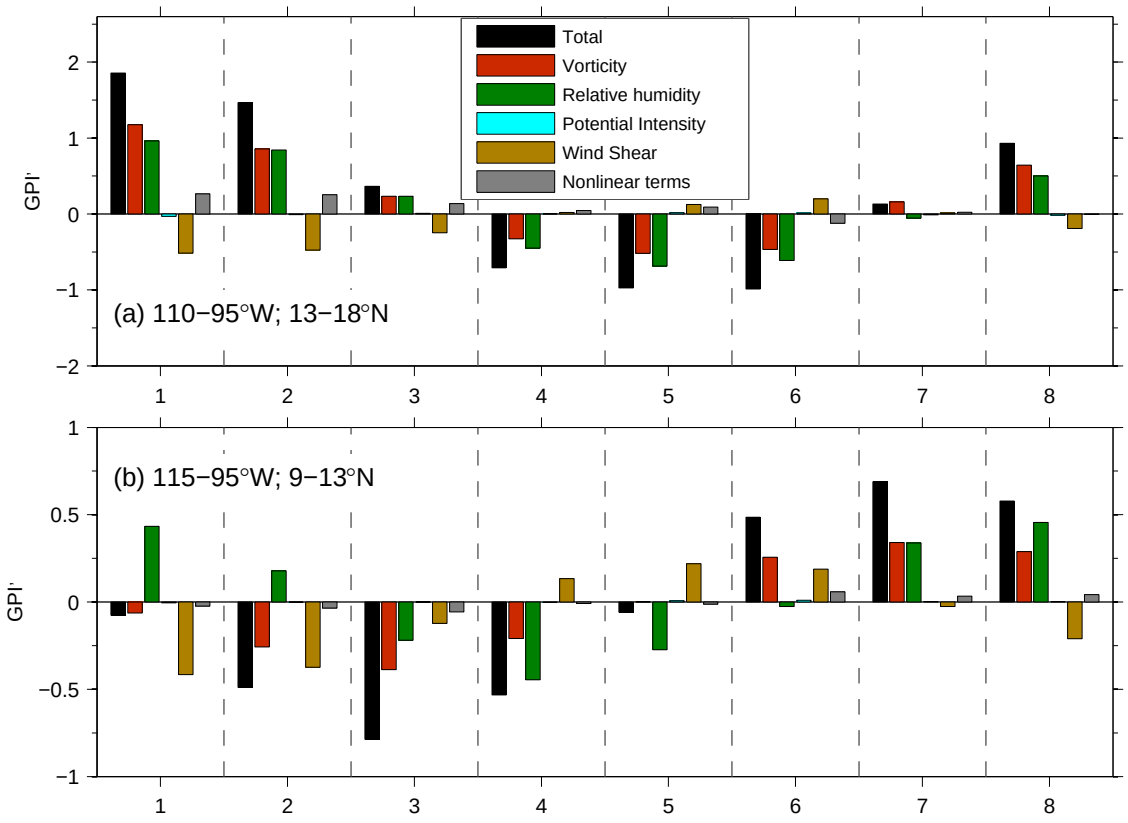

Figure 8 Same as in Fig. 6 but for HiRAM simulations over the two selected rectangle regions in Fig. 7e and 7l.